Modelling and measurement of the absolute level of power radiated by antenna integrated THz UTC photodiodes

Michele Natrella,[1] Chin-Pang Liu,[1] Chris Graham,[1] Frederic van Dijk,[2] Huiyun Liu,[1] Cyril C. Renaud,[1] and Alwyn J. Seeds[1,*]

[1]UCL Electronic and Electrical Engineering, Torrington Place, London WC1E 7JE, UK
[2]III-V Laboratory, 1, Avenue Augustin Fresnel, RD128 F-91767 Palaiseau Cedex, France
[*]a.seeds@ucl.ac.uk

Abstract: We determine the output impedance of uni-travelling carrier (UTC) photodiodes at frequencies up to 400 GHz by performing, for the first time, 3D full-wave modelling of detailed UTC photodiode structures. In addition, we demonstrate the importance of the UTC impedance evaluation, by using it in the prediction of the absolute power radiated by an antenna integrated UTC, over a broad frequency range and confirming the predictions by experimental measurements up to 185 GHz. This is done by means of 3D full-wave modelling and is only possible since the source (UTC) to antenna impedance match is properly taken into account. We also show that, when the UTC-to-antenna coupling efficiency is modelled using the classical junction-capacitance/series-resistance concept, calculated and measured levels of absolute radiated power are in substantial disagreement, and the maximum radiated power is overestimated by a factor of almost 7 dB. The ability to calculate the absolute emitted power correctly enables the radiated power to be maximised through optimisation of the UTC-to-antenna impedance match.

OCIS codes: (250.0250) Optoelectronics; (230.5170) Photodiodes; (350.5500) Propagation; (350.7420) Waves; (040.2235) Far infrared or terahertz; (130.5990) Semiconductors.

References and links

1. A. Beling, Z. Li, Y. Fu, H. Pan, and J. C. Campbell, "High-power and high-linearity photodiodes," IEEE Photonic Soc. 24th Annu. Meet. PHO 2011 **1**, 19–20 (2011).
2. H. Ito, T. Furuta, S. Kodama, and T. Ishibashi, "InP/InGaAs uni-travelling-carrier photodiode with 310 GHz bandwidth," Electron. Lett. **36**(21), 1809–1810 (2000).
3. C. C. Renaud, D. Moodie, M. Robertson, and A. J. Seeds, "High output power at 110 GHz with a waveguide Uni-travelling carrier photodiode," Conf. Proc. - Lasers Electro-Optics Soc. Annu. Meet. 782–783 (2007).
4. H. Ito, T. Nagatsuma, A. Hirata, T. Minotani, A. Sasaki, Y. Hirota, and T. Ishibashi, "High-power photonic millimetre wave generation at 100 GHz using matching-circuit-integrated uni-travelling-carrier photodiodes," Optoelectron. IEE Proc. **150**, 138–142 (2003).
5. H. Ito, F. Nakajima, T. Furuta, and T. Ishibashi, "Continuous THz-wave generation using antenna-integrated uni-travelling-carrier photodiodes," Semicond. Sci. Technol. **20**(7), S191–S198 (2005).
6. C. Renaud, M. Robertson, D. Rogers, R. Firth, P. Cannard, R. Moore, and A. Seeds, "A high responsivity, broadband waveguide uni-travelling carrier photodiode," Proc. SPIE **6194**, 61940C (2006).
7. H. J. Song, K. Ajito, Y. Muramoto, A. Wakatsuki, T. Nagatsuma, and N. Kukutsu, "Uni-travelling-carrier photodiode module generating 300 GHz power greater than 1 mW," IEEE Microw. Wirel. Compon. Lett. **22**(7), 363–365 (2012).
8. M. Natrella, E. Rouvalis, C.-P. Liu, H. Liu, C. C. Renaud, and A. J. Seeds, "InGaAsP-based uni-travelling carrier photodiode structure grown by solid source molecular beam epitaxy," Opt. Express **20**(17), 19279–19288 (2012).
9. E. Rouvalis, C. C. Renaud, D. G. Moodie, M. J. Robertson, and A. J. Seeds, "Continuous wave terahertz generation from ultra-fast InP-based photodiodes," IEEE Trans. Microw. Theory Tech. **60**(3), 509–517 (2012).
10. H. Eisele, "State of the art and future of electronic sources at terahertz frequencies," Electron. Lett. **46**(26), S8–S11 (2010).

#261680 Received 23 Mar 2016; revised 1 May 2016; accepted 2 May 2016; published 20 May 2016

11. C. Mann, "Practical challenges for the commercialisation of terahertz electronics," IEEE MTT-S Int. Microw. Symp. Dig. **2007**, 1705–1708 (2007).
12. A. J. Seeds, M. J. Fice, K. Balakier, M. Natrella, O. Mitrofanov, M. Lamponi, M. Chtioui, F. van Dijk, M. Pepper, G. Aeppli, A. G. Davies, P. Dean, E. Linfield, and C. C. Renaud, "Coherent terahertz photonics," Opt. Express **21**(19), 22988–23000 (2013).
13. M. Natrella, C.-P. Liu, C. Graham, F. van Dijk, H. Liu, C. C. Renaud, and A. J. Seeds, "Accurate equivalent circuit model for millimetre-wave UTC photodiodes," Opt. Express **24**(5), 4698–4713 (2016).
14. E. D. Palik, *Handbook of Optical Constants of Solids*, Illustrate (Academic, 1998), Vol. 3.
15. T. Pearsall and J. Hirtz, "The carrier mobilities in Ga0.47In0.53As grown by organo-metalic CVD and liquid-phase epitaxy," J. Cryst. Growth **54**(1), 127–131 (1981).
16. A. Katz, B. E. Weir, and W. C. Dautremont-Smith, "Au/Pt/Ti contacts to p-In0.53Ga0.47As and n-InP layers formed by a single metallization common step and rapid thermal processing," J. Appl. Phys. **68**(3), 1123–1128 (1990).
17. G. Reeves and H. Harrison, "Obtaining the specific contact resistance from transmission line model measurements," IEEE Electron. Dev. Lett. **3**(5), 111–113 (1982).
18. H. Berger, "Models for contacts to planar devices," Solid-State Electron. **15**(2), 145–158 (1972).
19. A. Rumiantsev, P. Sakalas, N. Derrier, D. Celi, and M. Schroter, "Influence of probe tip calibration on measurement accuracy of small-signal parameters of advanced BiCMOS HBTs," Bipolar/BiCMOS Circuits Technol. Meet. (BCTM), 2011 IEEE 203–206 (2011).
20. Anritsu, "Understanding VNA Calibration," http://anlage.umd.edu/Anritsu_understanding-vna-calibration.pdf.
21. A. J. Lord, "Comparing the accuracy and repeatability of on-wafer calibration techniques to 110GHz," Microw. Conf. 1999. 29th Eur. **3**, 28–31 (1999).
22. Cascade Microtech Application Note, "On-wafer vector network analyzer calibration and measurements," http://www.cmicro.com/files/ONWAFER.pdf.
23. Y. Yang, A. Shutler, and D. Grischkowsky, "Measurement of the transmission of the atmosphere from 0.2 to 2 THz," Opt. Express **19**(9), 8830–8838 (2011).
24. R. Appleby and H. B. Wallace, "Standoff detection of weapons and contraband in the 100 GHz to 1 THz region," IEEE Trans. Antennas Propagation **55**(11), 2944–2956 (2007).
25. C. Kittel, *Introduction to Solid State Physics*, 7th ed. (Wiley, 1996).

1. Introduction

Photonic THz emitters based on antennas integrated with uni-travelling carrier photodiodes (UTC-PDs) [1–9], are promising candidates for the realisation of sources within the lower part of the THz spectrum (100 GHz – 3 THz) [10–12]. The maximisation of the power extracted from a UTC is central to the successful realisation of a photonic THz emitter. When the UTCs are integrated with antennas, such maximisation entails the optimisation of the energy coupling between UTC and antenna. In the long history of RF and microwave antenna engineering, the impedance match between antenna and source has been shown to have a critical role. However, for antenna integrated photodiodes, this aspect has so far received little attention. To be able to calculate the absolute power radiated by antenna integrated UTCs and optimise the coupling efficiency between UTC and antenna, detailed knowledge of the UTC impedance is required. In our recent work [13] we have presented an experimental and semi-analytical study of waveguide UTC impedance and introduced an accurate circuit model verified up to 110 GHz. Although lumped element analysis of 15 μm long InP UTCs can, in principle, be employed up to about 400 GHz, where the effective wavelength is 20 times the UTC length, the results need to be validated to be extended up to such frequencies. In this paper we extend the knowledge of UTC impedance and photo-response up to 400 GHz, by performing for the first time 3D full-wave modelling of the detailed UTC-PD structure, including all epitaxial layers. Knowing the source and antenna impedance, and hence the coupling efficiency, up to the sub-millimetre wave frequency range, means that the absolute value of radiated power can be calculated up to such high frequencies. If the coupling efficiency is unknown, the radiated power cannot be predicted.

Furthermore we demonstrate prediction of the emitted power by modelling, using CST Microwave Studio, and measuring the power radiated by a 760 μm long bow-tie antenna integrated UTC at frequencies up to 185 GHz. We also show that the radiated power, calculated, based on the classical junction-capacitance/series-resistance concept, is in substantial disagreement with the measurements, which proves that a significant amount of radiated power can be lost due to sub-optimum photodiode to antenna impedance matching. The capability of predicting the radiated power correctly, raises the possibility of enhancing the radiated power by designing antennas approaching, as closely as possible, the maximum

#261680 Received 23 Mar 2016; revised 1 May 2016; accepted 2 May 2016; published 20 May 2016

power transfer condition, realised when the load impedance is equal to the complex conjugate of the source impedance. It is important to bear in mind that when the source impedance is complex, as is the case for the UTC, the minimisation of the reflection coefficient as a criterion to maximise the real power transferred to the load (antenna) cannot be employed. Complex conjugate matching has to be used instead.

While the antenna impedance is relatively easy to calculate and is established during the design stage, the modelling and evaluation of the UTC impedance is a far more challenging task. Knowing accurately the physical properties of all the semiconductor materials making up a UTC photodiode is essential to obtain valid results from modelling and such knowledge is difficult to achieve. UTCs contain ternary (e.g. InGaAs) and quaternary (e.g. InGaAsP) materials, with different element concentrations and different doping levels; the values of electrical permittivity and especially electrical conductivity for these materials can only be estimated. Furthermore, we showed in [13] that quantum mechanical effects governing the electron transport from the absorber to the collection layer, through the spacers, can affect the conduction properties in a way that, at a macroscopic scale, is reflected in changes in bulk material properties, such as resistivity and electrical permittivity. For these reasons, we employ the results of our previous work [13] which will help us assess and refine the material physical properties to employ in the full-wave modelling and simulation, which in turn enables the S_{11} and the UTC impedance to be evaluated up to frequencies not attainable by measuring equipment.

2. Device 3D full-wave modelling

The waveguide UTCs we model in this work were fabricated at III-V Lab and have the same structure as those studied in our recent paper [13], therefore the modelling here is also focused on 3 x 15 μm^2 and 4 x 15 μm^2 active area devices. The device epitaxial structure is given again in Table 1 while Fig. 1 shows photographs of two sample photodetectors, with active area equal to 3 x 15 μm^2 and 4 x 15 μm^2 respectively.

Table 1. Layer structure of the UTCs provided by III-V Lab.

Doping (cm^{-3})	Material	Function	Thickness (nm)
p + +	GaInAs	p-contact	200
p +	InP	Ridge Layer	1000
p-gradual	$In_{0.53}Ga_{0.47}As$	Absorber	120
n	Q	Spacer layer	–
n	Q	Spacer layer	–
n	InP	Depletion	300
n +	$Q_{1.17}$	Waveguide	300
n +	InP	n – contact	600
Fe	SI - InP	Substrate	–

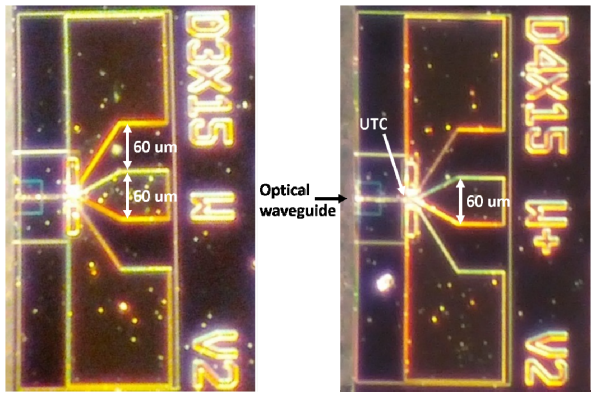

Fig. 1. Photograph of two sample UTCs, with 3 x 15 μm^2 and 4 x 15 μm^2 area. The devices are integrated with coplanar waveguide contact pattern for the use of air coplanar probes.

#261680 Received 23 Mar 2016; revised 1 May 2016; accepted 2 May 2016; published 20 May 2016

In [13] we introduced a new equivalent circuit model (Circuit 3), illustrated in Fig. 2, that provides very good agreement with UTC impedance and photo-response measured up to 110 GHz and 67 GHz respectively, for all of the four examined scenarios, e.g. 3 x 15 μm^2 UTC at 0 V and –2 V bias, 4 x 15 μm^2 UTC at 0 V and –2 V bias. Table 2 summarises the optimised circuit elements for the four scenarios. The spacers are modelled as two *RC* parallel circuits (R_2C_2 and R_3C_3). The R_4C_4 parallel represents the carrier collection layer, while R_1 takes into account the resistive effects of doped materials and ohmic contacts. Additional parameters employed to model the UTCs (such as electron overshoot velocity in the collection layer, diffusion constant of electrons in the absorber, thermionic emission velocity, carrier recombination lifetime in the absorber) can be found in [13].

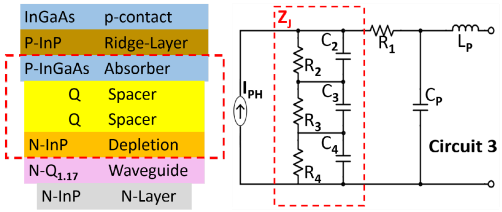

Fig. 2. Relation between the new equivalent circuit and the UTC structure.

Table 2. Summary of the equivalent circuit optimised parameters.

	$R_1(\Omega)$	$R_2(\Omega)$	$C_2(fF)$	$R_3(\Omega)$	$C_3(fF)$	$R_4(\Omega)$	$C_4(fF)$	$C_p(fF)$	$L_p(pH)$
3 x 15 μm^2 UTC at 0 V	15	265	105	125	81	3x10^5	67	1	16
3 x 15 μm^2 UTC at –2 V	15	265	85	125	70	3x10^5	60	1	16
4 x 15 μm^2 UTC at 0 V	(3/4)x 15	(3/4)x 265	(4/3)x 105	(3/4)x 125	(4/3)x 81	3x10^5	(4/3)x 67	1	16
4 x 15 μm^2 UTC at –2 V	(3/4)x 15	(3/4)x 265	(4/3)x 85	(3/4)x 125	(4/3)x 70	3x10^5	(4/3)x 60	1	16

The parasitic inductance L_p is principally due to the coplanar waveguide contact pads, deposited to enable the use of air coplanar probes. The value of C_p is very small and can be associated with the capacitive coupling between the n- and p-contact metal pads. Accurate evaluation of the parasitic effects in the structure can only be achieved by full-wave modelling, especially above 110 GHz.

The 3D full-wave modelling work has been performed in CST STUDIO SUITE. As reference source for the material properties, the CST STUDIO SUITE material database was employed together with the information available in [14,15] and in the on-line electronic archive of the Ioffe Physico-Technical Institute. The optimised parameters of the equivalent circuit and their relation with the device structure, discussed in [13] and here illustrated in Fig. 2, are also employed to set the material properties (i.e. conductivity and relative electrical permittivity) in CST.

The electrical conductivities and relative electrical permittivities of the layers contributing to the UTC series resistance are summarised in Table 3. The p- and n-ohmic contact resistances have been taken into account in the CST model by inserting thin layers of appropriate conductivity between the n/p-contact layers and the gold pads; we have used specific contact resistance values of 5.5 × 10^{-7} Ω cm^2 and 8 × 10^{-6} Ω cm^2 obtained by deposition of Ti/Pt/Au on Zn-doped 5 × 10^{18} cm^{-3} *p*-$In_{0.53}Ga_{0.47}As$ and S-doped 1 × 10^{18} cm^{-3} *n*-InP respectively, reported in the literature [16]. The ohmic contact resistance can be experimentally evaluated through transmission line model measurements [17,18] though it was not possible to carry out this type of measurements on our UTCs as no samples with the required contact pad patterns were available.

#261680 Received 23 Mar 2016; revised 1 May 2016; accepted 2 May 2016; published 20 May 2016

A CST model, as in Fig. 3, has been used to calculate the device DC resistance and verify that the conductivities given in Table 3 and the employed specific contact resistances actually produce a total device resistance of 15 Ω for the 3 x 15 μm^2 UTC.

Table 3. Conductivities used in the full-wave modelling for the layers contributing to the UTC series resistance. The relative electrical permittivity values are also shown, although they play a very marginal role for these layers.

Layer description	Thickness (nm)	Electrical conductivity ($\Omega^{-1}m^{-1}$)	Relative electrical permittivity
p-contact	200	19226	13.91
Ridge Layer	1000	3600	12.5
Waveguide	300	95000	13.12
n – contact	600	103000	12.5

It has to be noted that the assessment of the contribution provided to the device series resistance by the n-ohmic contact and the n-InP contact layer itself, is not a trivial geometrical problem. The area covered by the two n-metallisation pads is quite large (greater than 20 x 15 μm^2 each pad). Therefore, if the whole area was considered to calculate the n-ohmic contact resistance, then a value of only 1.3 Ω would be obtained. Actually, only a limited area of the pads is crossed by the electric current and hence the resistance offered by the ohmic contact is larger, i.e. 3.5 Ω. The current flows vertically through all the ridge layers and then through the InP n-layer to reach the n-metallisation. Here the intensity of the current flowing through the n-ohmic contact decreases gradually as we move further away from the p-ridge; in practice an effective area of 7.5 x 15 μm^2 for each of the two n-ohmic contacts can be identified, which would provide the same resistance of 3.5 Ω if uniformly crossed by the current. Absorber, spacer and depletion layers in the ridge have been here replaced by a layer of perfect electric conductor in this CST model, as they do not contribute to the device series resistance. This analysis highlights that having a high conductivity for the n-contact layer plays a critical role for the achievement of a low device series resistance.

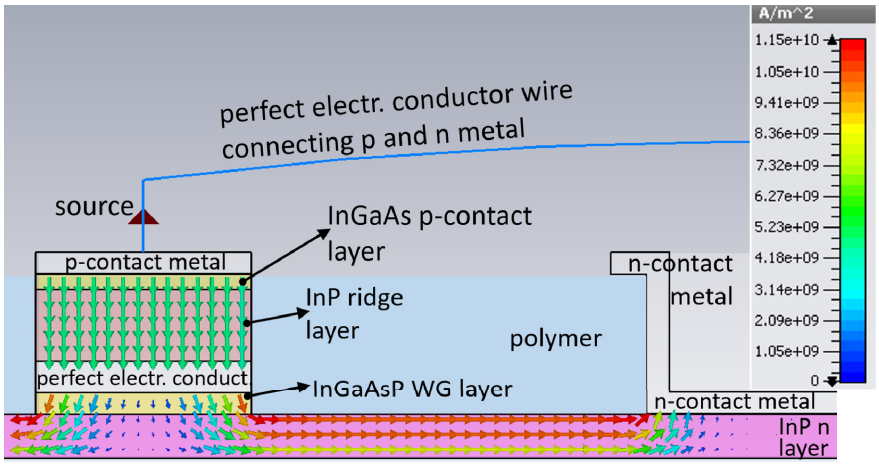

Fig. 3. Cross section of the UTC CST model, showing the current flowing through all the ridge layers and through the InP n-layer to reach the n-metallisation. The simulation shows that only a limited area of the interface between InP n-layer and n-metallisation is actually crossed by the current. Absorber, spacer and depletion layers in the ridge have been replaced by a layer of perfect electric conductor as they do not contribute to the device series resistance.

The CST model has also been used to verify whether the device series resistance actually scales down by a factor 3/4 for the 4 x 15 μm^2 UTC; it was found, as already suggested in [13], that the 4 x 15 μm^2 UTC series resistance is 12.7 Ω which is slightly larger than (3/4) x 15 Ω (= 11.2 Ω) and this is consistent with the fact that in reality only the resistance of the layers making up the ridge scales down by (3/4) while that of n-contact layer and n-ohmic

#261680 Received 23 Mar 2016; revised 1 May 2016; accepted 2 May 2016; published 20 May 2016

contact does not. The properties of the two spacers and the collection layer are dictated by the optimised circuit elements R_2, C_2, R_3, C_3, R_4 and C_4 of the equivalent circuit in Fig. 2, and are summarised in Table 4. It is important to bear in mind that these properties are not intended to represent the actual bulk properties of the materials making up the layers concerned but are the results of the model we have introduced in [13] to explain the effects observed in the experimental data. As can be seen in Table 4, the relative electrical permittivity of the layers, except the absorption layer, is slightly different for the two different bias values (0 V and –2 V). This takes into account the small capacitance change introduced by the applied reverse voltage. Although the changes in capacitance are due to variations of the depletion region thickness, we have preferred to maintain the model geometry unchanged and account for the effect by means of an equivalent permittivity variation. Since the absorption layer only provides a marginal resistive contribution, its permittivity was not changed. The passivation layer was Benzocyclobutene (BCB) and was modelled as a polymer dielectric with an electrical permittivity of 2.5. The substrate was modelled with standard 12.5 permittivity indium phosphide (InP) while for the metal pads the default CST gold model (conductivity of 4.561×10^7 $(\Omega m)^{-1}$) was employed. Very thin layers of platinum (conductivity of 9.52×10^6 $(\Omega m)^{-1}$) and titanium (conductivity of 2.32×10^6 $(\Omega m)^{-1}$) were also included in the model between the polymer and the CPW gold but were not inserted between the UTC n/p- contact layers (InGaAs/InP) and the gold because at these locations, as mentioned previously, ad hoc layers were introduced to take the ohmic contact resistances into account.

Table 4. Material properties of the two spacers and the collection layer derived by the optimised circuit elements R2, C2, R3, C3, R4 and C4 of Circuit 3. The absorber properties are also shown, although this layer only provides a marginal resistive contribution.

Layer description	Thickness (nm)	Electrical conductivity ($\Omega^{-1}m^{-1}$)	Relative electrical permittivity (0 V bias)	Relative electrical permittivity (–2 V bias)
Absorber	120	4005	13.91	13.91
Spacer Q	–	1.26	3.95	3.20
Spacer Q	–	2.67	3.05	2.63
Collector	300	0.02	50.45	45.18

The CST model including the whole of the cleaved chip and the CPW pads is illustrated in Fig. 4. Figure 5 shows additional details of the area near the UTC, including the n-contact layer mesa and the optical waveguide, while a further magnified cross section view is given in Fig. 6, showing details of the layers making up the ridge.

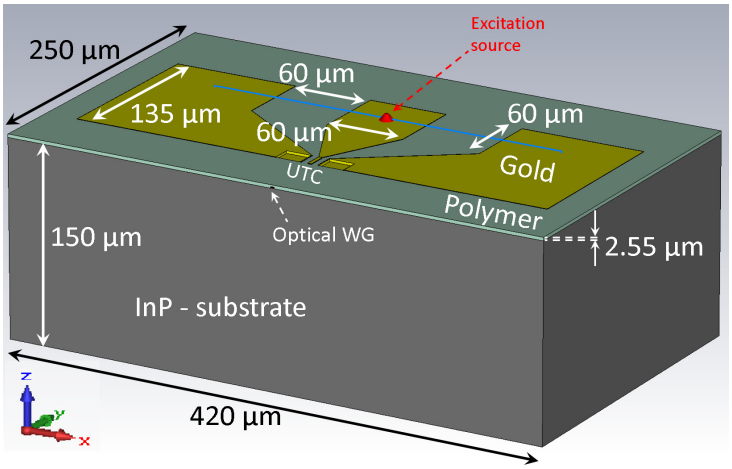

Fig. 4. CST model including the whole of the cleaved chip and the CPW pads.

#261680 Received 23 Mar 2016; revised 1 May 2016; accepted 2 May 2016; published 20 May 2016

Since the chip was placed on a brass mount during the measurement, a perfect electric conductor (PEC) plane was used as boundary condition underneath the InP substrate (Z_{min}), while all the other boundaries were surrounded by vacuum. The excitation source, highlighted in red in Fig. 4, was placed on the CPW signal pad and connected to the ground pads through ideal one-dimensional PEC wires (blue lines in Fig. 4) which introduced no parasitic capacitance; to reduce the current loop inductance introduced by the wires, the loop areas were kept as small as possible. The excitation source is a CST "discrete port", essentially representing a Norton (or Thevenin) equivalent with a 50 Ω impedance. The CST discrete ports provide accurate results when their size is much smaller than the wavelength; in our model the discrete port is 1 µm long. It should be noted that the hardware used for this work enabled the simulation of very large models, up to a few hundred million mesh cells, containing geometrical features extremely small compared to the bounding box size; for instance, the extremely thin spacer layers shown in Fig. 6, were discretized by 4 mesh lines in the vertical direction.

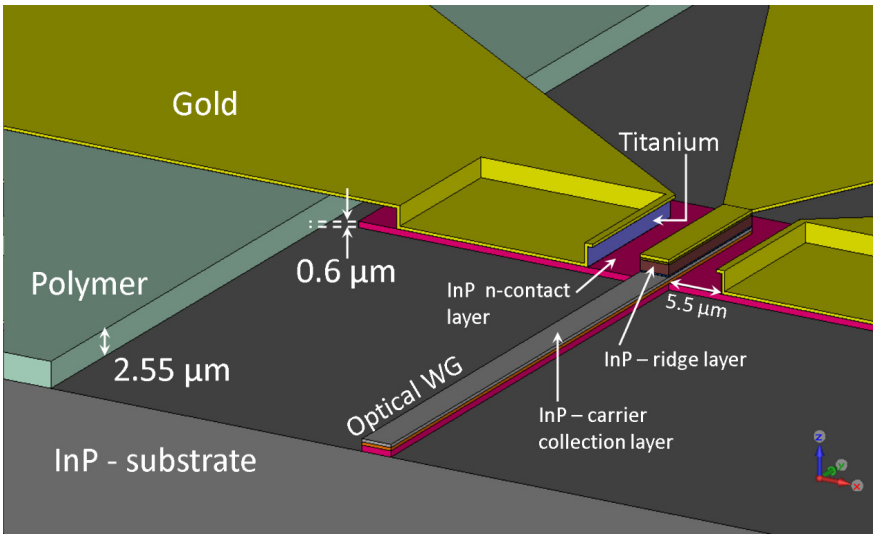

Fig. 5. Model details of the area near the UTC, including the n-contact layer mesa and the optical waveguide.

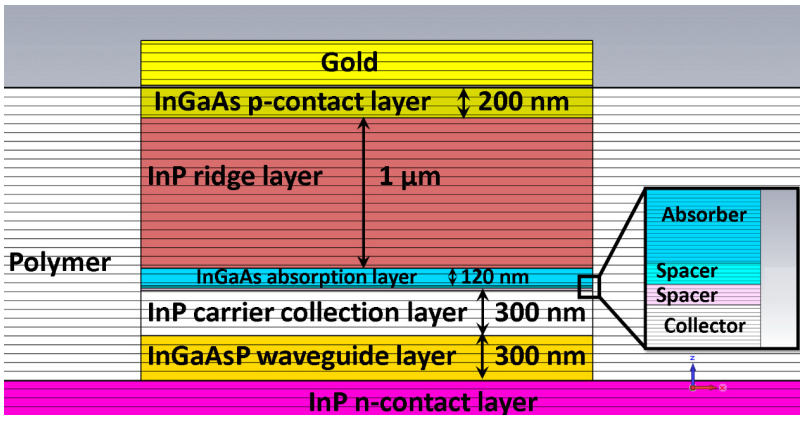

Fig. 6. Magnified cross section view showing details of the layers making up the UTC ridge.

#261680 Received 23 Mar 2016; revised 1 May 2016; accepted 2 May 2016; published 20 May 2016

3.1 S_{11} and impedance 3D full-wave modelling

The S_{11} and impedance of the 3 x 15 μm^2 area UTC at 2 V reverse bias were calculated in CST up to 400 GHz and are shown in Fig. 7, together with the experimental data up to 110 GHz, reported in [13], and with the results obtained using the new circuit shown in Fig. 3, also introduced in [13]. The values shown in Table 2 are employed for the circuit parameters; these parameters include the value of 16 pH for the parasitic inductance L_p which resulted from fitting the S_{11} measured in the W-band [13]. We investigated the effect of the CPW pads on the S_{11} both experimentally and using CST. We found that the CPW pads have no or small effect on the measured S_{11} below 67 GHz, whereas they start having a significant effect in the W-band; the effect becomes dramatic above 110 GHz. The CST modelled S_{11} and impedance shown in Fig. 7 have been calculated in CST excluding the effect of the CPW pads and therefore refer to the UTC alone. This is important in view of the UTC to antenna matching optimisation, since the impedance seen from the terminals of an antenna integrated with the UTC does not include the CPW pads.

The magnitudes of the measured S_{11} and the S_{11} obtained with CST and the equivalent circuit are all in excellent agreement up to 90 GHz and good agreement between 90 GHz and 110 GHz. The phases are all in excellent agreement up to 67 GHz, then measurement and circuit phases maintain good agreement up to 110 GHz, while CST phase begins to depart. Above 110 GHz the disagreement between the equivalent circuit and CST S_{11} becomes increasingly significant. This disagreement is entirely due to the value of the inductance L_p in the circuit which is too high (16 pH), as can be seen clearly from the reactance in Fig. 7 which switches from capacitive (i.e. < 0) to inductive (i.e. > 0) at 255 GHz for the circuit while it is still slightly capacitive at 400 GHz for the CST result. Importantly, if L_p is reduced to 6.5 pH, the S_{11} and impedance obtained with CST and the circuit are identical up to 400 GHz. As mentioned above the value of 16 pH for L_p in [13] resulted from the need to force the circuit S_{11}, particularly its phase, to match the S_{11} measured between 75 GHz and 110 GHz. However, as mentioned previously, the S_{11} measured in the W-band is affected by the effect of the CPW and most importantly by inevitable uncertainty of the SOLT calibration on wafer at these frequencies [19–22]. It is important to bear in mind that for the other three scenarios (e.g. 3 x 15 μm^2 UTC at 0 V, 4 x 15 μm^2 UTC at 0 V and 4 x 15 μm^2 UTC at –2 V), as well as for the result in Fig. 7, the amended 6.5 pH inductance would provide excellent agreement between circuit and CST results up to 400 GHz.

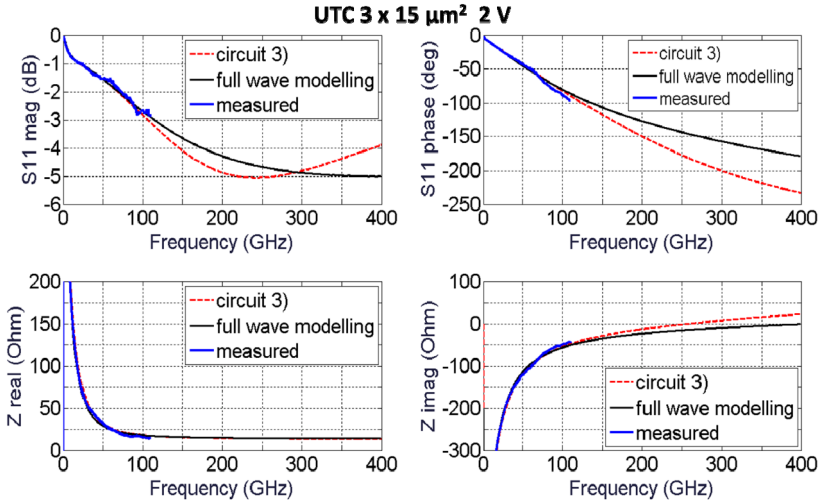

Fig. 7. S_{11} and impedance of the 3 x 15 μm^2 area UTC at –2 V bias, calculated using CST, compared with the experimental data and with the results obtained using the equivalent circuit (including the overestimated parasitic inductance L_p = 16 pH). The amended value of 6.5 pH for L_p provides excellent agreement between circuit and CST up to 400 GHz.

#261680 Received 23 Mar 2016; revised 1 May 2016; accepted 2 May 2016; published 20 May 2016

3.2 Frequency photo-response 3D full-wave modelling

3D full-wave modelling was also employed to calculate the UTC frequency dependent photo-response. The frequency response calculated in CST only represents the RC-limited response; the transit-time limited response contribution is incorporated using the transit-time responses calculated in [13]. For the modelling of the frequency response, the discrete port used as excitation source for the S_{11} calculation was replaced with a 50 Ω load, representing the lightwave component analyser input impedance to which the RF power generated by the UTC is delivered. Also, an ideal current source was placed across collection layer, spacers and absorber, connecting the heavily doped waveguide and ridge layers. The effect of the overestimated parasitic inductance (L_p = 16 pH) on the UTC photo-response is shown in Fig. 8; here the RC-limited response calculated with full-wave simulation is compared with the experimental data [13] and with the circuit RC-limited response for both the overestimated value of parasitic inductance (L_p = 16 pH) and the amended value (L_p = *6.5 pH*). As for the case of S_{11} and impedance calculation, the too high initial value of the inductance L_p (16 pH) is entirely responsible for the disagreement between the circuit and CST results. Remarkably, as for S_{11} and impedance, the amended value of 6.5 pH for L_p also provides a very good agreement between Circuit 3 and CST RC-limited frequency response up to 400 GHz, as also shown in Fig. 8. The reason why a greater value of inductance L_p provides a better power transfer to the 50 Ω R_L up to at least 300 GHz is that, such an inductance (16 pH) tunes the capacitive component of the UTC reactance more efficiently than the smaller value (6.5 pH).

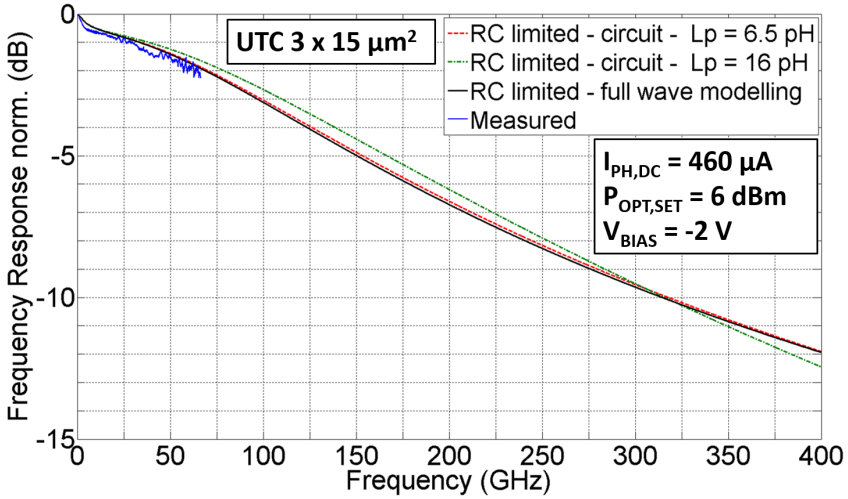

Fig. 8. Comparison between RC-limited response calculated with full-wave simulation (continuous black line) and experimental data (continuous blue line). The RC-limited response calculated with the equivalent circuit, using both the initial value of parasitic capacitance L_P = 16 pH (dash-dot green line) and the amended value 6.5 pH (dashed red line) are also shown.

If we now use the CST RC-limited response to calculate the overall UTC frequency response, by incorporating the transit-time limited response calculated in [13], we obtain the results shown in Fig. 9 for the 3 x 15 µm^2 device.

#261680 Received 23 Mar 2016; revised 1 May 2016; accepted 2 May 2016; published 20 May 2016

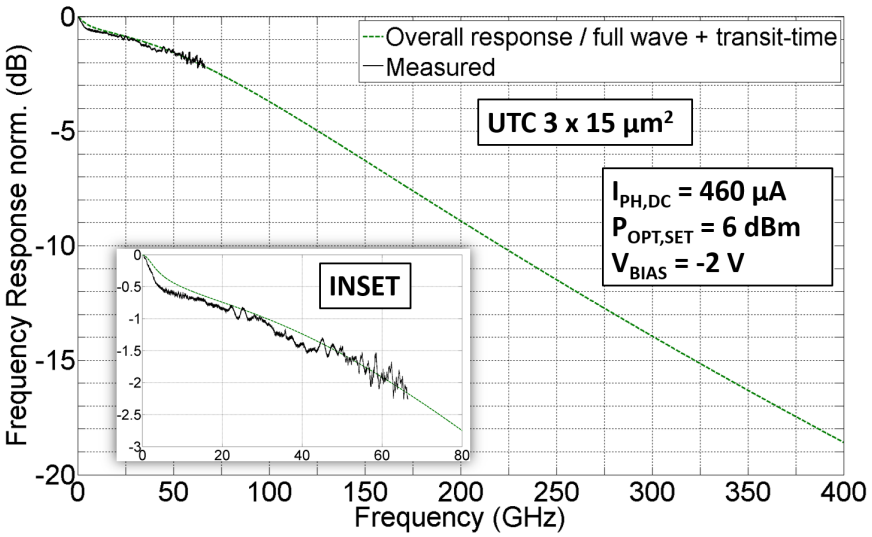

Fig. 9. Comparison between measured frequency photo-response and overall frequency photo-response calculated combining the full-wave modelling RC-limited response with the transit-time limited responses calculated in [13], for the case of a 3 x 15 µm^2 area UTC. The inset is a magnified view of the responses in the frequency range 0 GHz to 80 GHz.

4. Modelling and measurement of the absolute power radiated by a bow-tie antenna integrated UTC

III-V Lab also fabricated a 3 x 15 µm^2 area UTC integrated with a bow-tie antenna with a gold screen deposited underneath the InP substrate, shown in Fig. 10(a); we measured the substrate thickness which was 200 µm. The gold screen was not intended to operate as a ground plane for the antenna emission, therefore the whole antenna chip did not represent an optimum design for radiation with a ground plane. However, the antenna represented an opportunity to investigate whether the knowledge of the UTC impedance, in conjunction with antenna full-wave modelling, could provide a good prediction of the absolute level of power radiated over the frequency range. Considering the antenna length (about 760 µm) and the InP relative electrical permittivity (12.5), the theoretical half-lambda resonance of the antenna on a semi-infinite InP substrate, would be around 76 GHz.

The power emitted by the antenna integrated UTC in Fig. 10(a), was measured between 65 GHz and 185 GHz with a basic heterodyne experimental arrangement using two free running lasers. The optical power applied to the UTC was measured with a power meter and was 50 mW. The UTC was still operating in the linear region and no sign of saturation was observed. The UTC was biased at –2 V and exhibited a DC photocurrent of 7.2 mA, corresponding to a 0.144 A/W responsivity. A Thomas Keating (TK) power meter system was used to measure the radiated power. The antenna chip was also modelled in CST, as shown in Fig. 10(b), over the frequency range 50 GHz to 185 GHz.

#261680 Received 23 Mar 2016; revised 1 May 2016; accepted 2 May 2016; published 20 May 2016

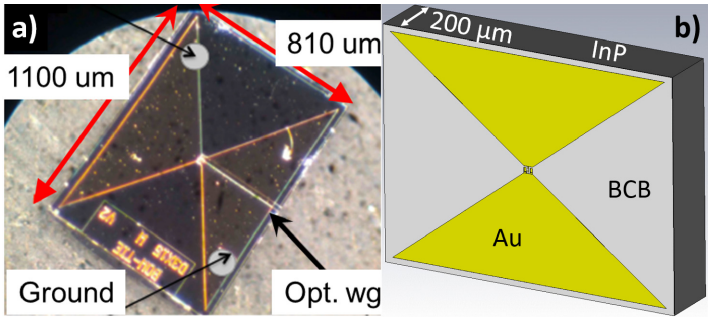

Fig. 10. a) Bow-tie antenna integrated UTC with a ground plane, provided by III-V Lab. The photodetector area is 3 x 15 µm^2 and the antenna-chip approximate geometrical details are shown in the picture; b) CST model of the bow-tie antenna with a gold ground plane.

The total power emitted by an antenna depends on the efficiency of energy coupling with the driving source and on the radiation efficiency. The former defines the fraction of power made available by the source that is accepted by the antenna, while the latter determines the fraction of power accepted by the antenna that is coupled into free space. The antenna directivity, on the other hand, describes the angular distribution of the radiated power.

The bow-tie Antenna 3D radiation pattern (directivity in dBi) calculated in CST, is shown in Fig. 11 for four frequencies of interest, i.e. 67.5 GHz, 116.3 GHz, 145 GHz and 180 GHz. The radiation patterns show how part of the emitted power, especially at 116.3 GHz, is radiated almost along the XY plane, or at least at very shallow angles, and would not be captured by a power meter positioned in front of the antenna in a real measurement. For this reason the power radiated within different rectangular solid angles along the Z direction has also been calculated, to enable a more realistic comparison with the experimental results.

The maximum transfer of power between source and antenna occurs at the frequencies for which the antenna impedance is equal to the source (UTC) impedance complex conjugate. Therefore local maxima of radiated power should be expected at the frequencies where source and antenna reactance have similar absolute value and opposite sign and the impedance real parts are comparable. The level of radiated power is also affected by other factors including radiation efficiency, solid angle considered for the radiated power calculation and transit-time limited response of the UTC.

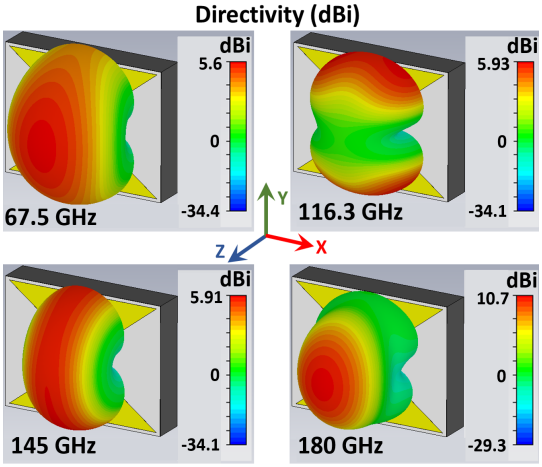

Fig. 11. Bow-tie antenna 3D radiation pattern calculated in CST.

In Fig. 12 we plot the measured radiated power and the radiated power calculated when the UTC impedance is simply taken into account employing the classical junction-

#261680 Received 23 Mar 2016; revised 1 May 2016; accepted 2 May 2016; published 20 May 2016

capacitance/series-resistance concept; in this case the photodiode reactive component is only attributed to a single capacitance of 17 fF, i.e. the junction capacitance based on the device geometry and material properties. The power radiated at each frequency by an antenna is proportional to the squared amplitude of the current flowing into the antenna at that frequency; on the other hand the current flowing into the antenna depends on the match/mismatch between antenna impedance and source impedance. The measured 7.2 mA DC photocurrent can be used as a reference level and the transit-time limited response used to calculate the overall photo-current response in Fig. 9, can be considered to take the transit-time effect into account. The radiated power was calculated for different rectangular solid angles along the Z axis. Such solid angles are defined by two planar angles relative to the Z axis, one in the XZ plane and the other in the YZ plane. For instance the 90 x 90 degrees rectangular solid angle in Fig. 12 is identified by an angle of 45° with respect to the Z axis, lying within the XZ plane, and an angle of 45° in the YZ plane. The solid angle "TK window" in Fig. 12 refers to the solid angle subtended by the 40 x 30 mm^2 Thomas Keating window with respect to the emitter positioned 33 mm apart; the solid angle "TK window" is hence identified by a 31.2° angle in the XZ plane and 24.4° in the YZ plane.

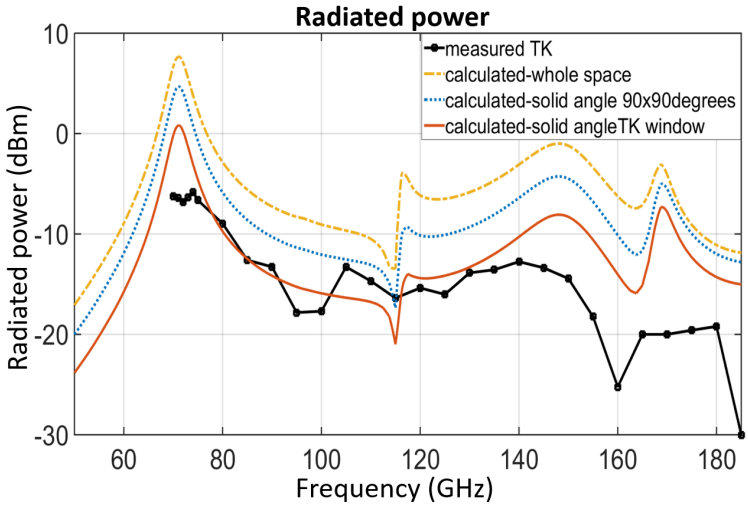

Fig. 12. Comparison between measured radiated power and radiated power calculated when the UTC impedance is taken into account using the classical junction-capacitance/series-resistance concept. The power is also calculated within rectangular solid angles along the Z axis.

The trends of measured and calculated power over the frequency range in Fig. 12 seem correlated; the peaks of measured power at 74 GHz and 140 GHz seem to correspond to the peaks of calculated power at 71 GHz and 148 GHz, and the narrow peak of measured power at 105 GHz seem to correspond to the feature in the calculated power around 115 GHz. However, the peak of radiated power calculated within the solid angle "TK window" at 71 GHz is 6.6 dB greater than the peak of power measured at 74 GHz (0.8 dBm vs. −5.8 dBm, i.e. 1202 μW vs. 262 μW). The peak of radiated power calculated within the solid angle "TK window" at 148 GHz is 4.7 dB greater than the peak of power measured at 140 GHz (−8.1 dBm vs. −12.8 dBm, i.e. 155 μW vs. 53 μW). This disagreement is significant and proves that a design based on the classical junction-capacitance/series-resistance assumption would have led to a substantial overestimation of the radiated power obtainable.

To perform a thorough calculation of the absolute level of power emitted by the antenna, the coupling efficiency between the antenna and the UTC must be properly taken into account; this can now be evaluated using the results of the experimental and numerical analysis of UTC impedance, discussed above and in [13]. The real and imaginary parts of the antenna impedance are plotted in Fig. 13 and compared with those we obtained for the 3 x 15 μm^2 area UTC at −2 V bias.

#261680 Received 23 Mar 2016; revised 1 May 2016; accepted 2 May 2016; published 20 May 2016

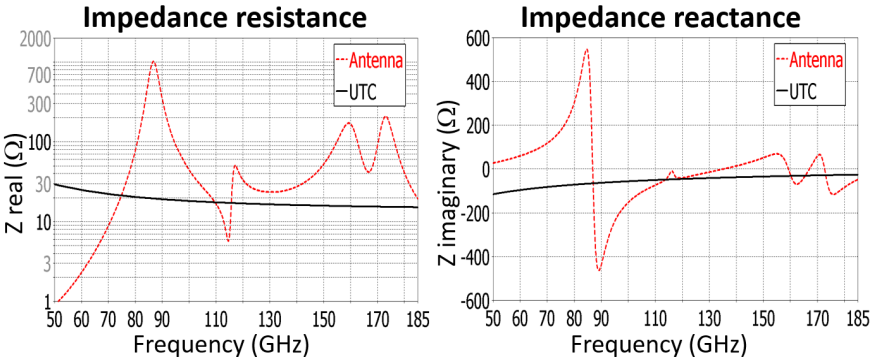

Fig. 13. Comparison between real and imaginary parts of the bow-tie antenna impedance and those measured and calculated for the 3 x 15 μm^2 area UTC at –2 V bias.

In Fig. 14 we plot the measured radiated power and the radiated power calculated when the UTC to antenna coupling efficiency is based upon our knowledge of the UTC impedance, plotted in Fig. 13. The main maxima of power accepted by the antenna occur at frequencies where the imaginary parts of UTC and antenna impedance have about same absolute value and opposite sign and the real parts are comparable (i.e. 67 GHz, 145 GHz, 168 GHz), as reflected in the calculated emitted power plotted in Fig. 14. On the other hand there are frequencies where, despite the impedance imaginary parts having similar absolute value and opposite sign, there is no peak of radiated power because the impedance real parts are greatly different; this situation is verified at 87 GHz, where the impedance real part is 20 Ω for the UTC and over 1 kΩ for the antenna, and at 173 GHz where the impedance real part is 15 Ω for the UTC and 190 Ω for the antenna. The importance of the coupling efficiency between source and antenna can be seen at 180 GHz where the radiated power calculated within an increasingly narrow solid angle does not show any maximum although the directivity pattern is favourable, as shown in Fig. 11, and the impedance real parts of UTC and antenna are fairly close (15 Ω vs 40 Ω). The reason is that the UTC and antenna reactance are both capacitive at 180 GHz, therefore little power is accepted by the antenna. The small sharp local maximum calculated at 116 GHz, is due to a rapid increase of the antenna resistance that equals the UTC resistance, while the antenna reactance peaks to zero. This maximum tends to disappear as an increasingly narrow solid angle is considered, because, at this frequency, the power is mostly radiated at very shallow angles with respect to the antenna plane, as can be seen in Fig. 11.

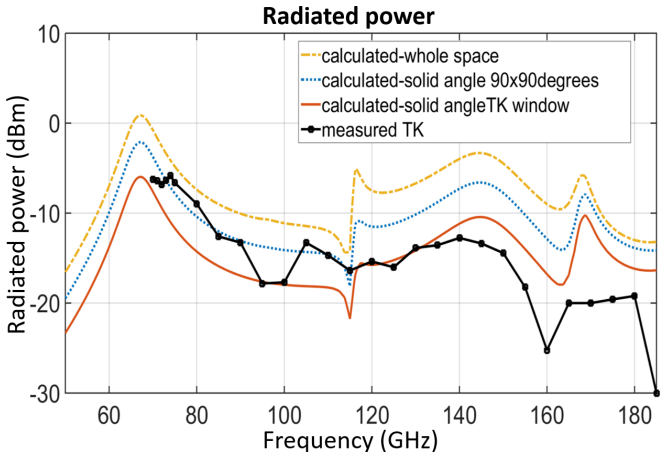

Fig. 14. Comparison between measured radiated power and radiated power calculated when the UTC to antenna coupling efficiency is based on our achieved knowledge of the UTC impedance, plotted in Fig. 13.

#261680 Received 23 Mar 2016; revised 1 May 2016; accepted 2 May 2016; published 20 May 2016

A direct comparison between the radiated power calculated in CST within the solid angle "TK window" and the measured radiated power, is shown in Fig. 15 in μW on a linear scale. The trends of measured and calculated power over the frequency range are clearly correlated and show a good agreement. The peaks of measured power at 74 GHz and 140 GHz seem to correspond to the peaks of calculated power at 67 GHz and 145 GHz. The small peak of measured power at 105 GHz seems to correspond to the feature in the calculated power around 115 GHz; we found that both position and prominence of this calculated feature are quite sensitive to the chip width and length. The measured peak at 74 GHz and the calculated peak at 67 GHz have very similar magnitude, i.e. 262 μW (−5.8 dBm) vs 253 μW (−5.9 dBm). The measured peak at 140 GHz and the calculated peak at 145 GHz have magnitude of 53 μW (−12.7 dBm) and 90 μW (−10.4 dBm), i.e. differ by 2.3 dB. The sharp peak calculated at 168 GHz was barely detected in the measurements, which were not performed above 185 GHz as the detected signal reached the minimum level detectable by the TK power meter, whose electrical noise-equivalent power (NEP) equals 5μW/Hz^{½}. Although a peak of water vapour absorption is present near 175 GHz [23,24], as high as 100 dB/km in humid conditions, its influence on the 33 mm propagation path length is negligible. The ohmic losses within the titanium layer may have influenced the power measured at higher frequencies. We investigated numerically the effect of thin (10 to 30 nm) titanium layers under the antenna gold, using the reported value 2.32 x 10^6 S/m [25] of titanium bulk conductivity; we found that the additional ohmic losses related to the titanium did reduce the calculated peak at 168 GHz in particular, but by less than 10%, which still cannot explain the discrepancy with the measurement at this frequency. It is worth noting that the calculated peak at 168 GHz is related to a fast local variation in the antenna impedance, as can be seen in Fig. 13. At this frequency the antenna impedance real part exhibits a narrow and pronounced dip which makes it closer to the UTC impedance real part; in addition the antenna reactance exhibits a rapid increase which allows the complex-conjugate matching condition to be approached between antenna and UTC. Additionally, we found that both amplitude and position of the calculated peak at 168 GHz are noticeably sensitive to the chip width and length. It is the authors' opinion that this pronounced local variation of the antenna impedance at 168 GHz, responsible for the peak of calculated emitted power, is due to a fortunate combination of effects related to the exact geometrical details of the model and is barely perceivable in the real antenna chip, as is the maximum of measured power around 168 GHz. As a final remark, we note that a slower than estimated transit time limited response, for the UTC integrated with the bow-tie antenna, could account for the measured emitted power being more damped at higher frequencies.

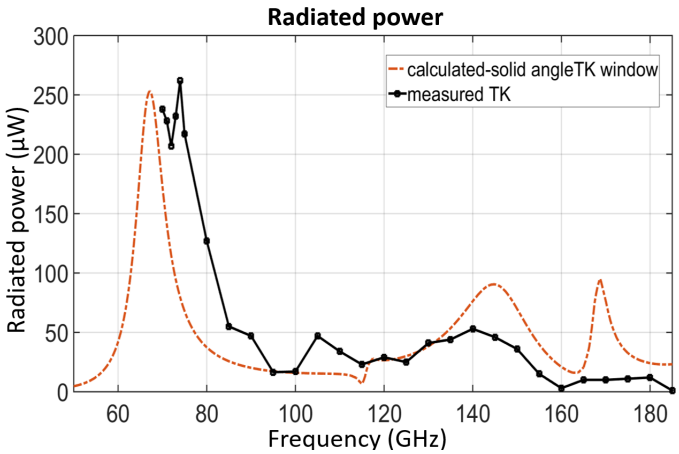

Fig. 15. Comparison between measured radiated power and radiated power calculated within the rectangular solid angle (31.2° x 24.4°) subtended by the 40 x 30 mm^2 Thomas Keating window.

#261680 Received 23 Mar 2016; revised 1 May 2016; accepted 2 May 2016; published 20 May 2016

Following these considerations and bearing in mind the level of difficulty involved in predicting the absolute power radiated by a system involving so many variables, the agreement between experimental and numerical results shown in Fig. 15 can be deemed very satisfactory. An accurate analysis of the absolute power emitted from an antenna integrated photodetector has not been reported before, including 3D full-wave modelling of photodetector and antenna and taking into account the effect of the actual impedance match/mismatch between photodetector and antenna.

4. Conclusions

The literature of RF and microwave antenna engineering shows how fundamental the source-to-antenna impedance match is, to maximise the power radiated by antennas. In the more recent context of photonic THz emitters based on antenna integrated photodiodes, this aspect has so far received little attention. An emitter made up of a highly directive and efficient antenna integrated with a high power photodiode, could still be unable to radiated high levels of power if the impedance match between source and antenna is ignored, as most of the power generated by the photodiode could be simply rejected by the antenna. In order to optimise the photodiode-to-antenna coupling efficiency, knowledge of the source (PD) impedance is necessary; with no knowledge of the source impedance the absolute power radiated by an antenna cannot be calculated.

In this paper we have performed for the first time 3D full-wave modelling of a detailed UTC-PD structure, including all epitaxial layers, and calculated the UTC impedance and S_{11} up to 400 GHz, frequencies not attainable by measuring equipment. This work is indispensable to extend to higher frequencies our previous work on semi-analytical modelling of the UTC impedance, limited to below 110 GHz.

An additional new contribution of this work is that we have provided evidence, for the first time, that proper evaluation of the UTC impedance and UTC-to antenna impedance match can allow accurate calculation of the absolute power radiated by an antenna integrated UTC over the frequency range. We have demonstrated successful prediction of the absolute emitted power by modelling and measuring a 760 μm long bow-tie antenna integrated UTC up to 185 GHz. We have also shown that if the UTC-to-antenna coupling efficiency is modelled based on the classical junction-capacitance/series-resistance concept, calculated and measured radiated power are in substantial disagreement.

The capability of calculating the absolute emitted power correctly raises the possibility to maximise the radiated power via optimisation of UTC-to-antenna impedance match. We can effectively design antennas with ad hoc complex impedance, realising complex-conjugate matching with the UTC.

Acknowledgments

This work has been supported by the United Kingdom Engineering and Physical Sciences Research Council (EPSRC), grant number: EP/J017671/1.

#261680 Received 23 Mar 2016; revised 1 May 2016; accepted 2 May 2016; published 20 May 2016